Post-Print

When citing this work, cite the original published paper.

End-of-Life Disposal of Libration Point Orbit Missions: the case of Gaia

Roberto Armellin[a,1,*], Mirco Rasotto[b,2], Pierluigi Di Lizia[c,3], Florian Renk[d,4]

[a] *Aeronautics, Astronautics and Computational Engineering Unit, University of Southampton, Highfield campus, SO17 1BJ, Southampton, United Kingdom*
[b] *Dinamica Srl, Piazza della Repubblica 10, 20121 Milano, Italy*
[c] *Department of Aerospace Science and Technology, Politecnico di Milano, Via La Masa 34, 20156 Milano, Italy*
[d] *European Space Operations Center, European Space Agency, Robert-Bosch-Str. 5, 64293 Darmstadt, Germany*

Abstract

This work investigates end of life disposal options for libration point orbit missions. Three different options are presented: the first one considers spacecraft's re-entry in Earth's atmosphere, the second one concerns the impact on the Moon, whereas the third one consists in the injection of the spacecraft into a heliocentric graveyard orbit. The disposal design is formulated as a multi-objective optimization problem in order to take into account other goals in addition to propellant consumption minimization. The disposal of Gaia mission is used as test case throughout the paper.

Keywords: End of life disposal; Libration Point missions; Space debris; Gaia mission

[*]Corresponding author (tel: +44-23-8059-2597, fax: +44-23-8059-3058)

Email addresses: roberto.armellin@soton.ac.uk (Roberto Armellin), rasotto@dinamicatech.com (Mirco Rasotto), pierluigi.dilizia@polimi.it (Pierluigi Di Lizia), florian.renk@esa.int (Florian Renk)

[1]Lecturer
[2]Junior Engineer
[3]Postdoc Fellow
[4]Mission Analyst

1. Introduction

Libration point orbit (LPO) missions are defined as those in which the spacecraft orbits around one of the five libration points of the Sun-Earth system. These librations points (or Lagrange points) have the property of being at rest with respect to a pair of primaries, which makes them particularly appealing for a number of space applications. More specifically, LPOs around the collinear libration points L_1 and L_2 (Szebehely and Williams, 1964) present very well-known advantages in terms of thermal stability, observation and communication geometries stability, and minimum level of required budget for on-orbit maintenance maneuvers (Bastante et al., 2003). For these reasons, the number of LPO missions around these two points has increased over the last 15 years and a further growth is expected within next years. On the other hand, third collinear point L_3, as well as triangular points L_4 and L_5, have never been used, and there are only few works on mission design to these points. Although they can be interestingly exploited by space weather observatories as shown by Akioka et al. (2005), this lack is due in part to the large ΔV costs (Prado, 2002) and to the large communication range (1 AU from the Earth for L_4 and L_5). The scope of this study is then restricted only to LPOs around L_1 and L_2, while future developments might focus on the disposal strategies for missions around the remaining libration points.

The intrinsic dynamical instability around these two points produces a sort of "self-cleaning behaviour", for which an uncontrolled spacecraft at the end of its operative life will inevitably leave its operative orbit. This fact suggests that no protected regions have to be defined for LPO missions in L_1 and L_2. Nonetheless, long-term propagations have highlighted the possibility for these departing trajectories to come back to the Earth-Moon system, with potential interferences with LEO and GEO protected regions, as well as reentries in the Earth's atmosphere with large casualty area (Di Mauro et al., 2013). In light of this consideration, an adequate end-of-life (EoL) disposal strategy for LPO missions is always recommended.

Since the launch of the first LPO mission, the International Sun-Earth Explorer (ISEE-3), performed by NASA in 1978, and despite the growth of the number of LPO missions in the last years, few works have focused on the design of their disposal. Most of them have been disposed into heliocentric graveyard orbits (Garcia et al., 2012). Two more recent examples are represented by the ESA's missions, Herschel and Planck: launched together in

May 2009, the first was decommissioned in May 2013, whereas for the latter the final deactivation command was sent in October 2013. Both spacecraft were placed into heliocentric orbits, after about four years of operative life (Schmidt and Keck, 2014).

To authors' knowledge, Olikara et al. (2013) is the first research paper where different options available for the disposal of LPO missions are analyzed. The properties of the circular restricted three-body problem (CR3BP) dynamics are exploited to design low-cost decommissioning maneuvers to either inject spacecraft into heliocentric orbit or to impact it on a celestial body. More recently, a set of publications on the topic appeared as an outcome of the ESA (parallel) study "End-of-Life Disposal Concepts for Lagrange-Points and HEO Missions" lead by Dinamica Srl and University of Southampton, respectively (Di Mauro et al., 2013; Colombo et al., 2013). In Colombo et al. (in press) and Alessi et al. (2014) the same disposal options introduced in Olikara et al. (2013) are first designed in the CR3BP, and a subset is refined in a high-fidelity model. In Armellin et al. (2014) the disposal design is formulated as a global optimization problem in which a high accuracy model of the dynamics is employed. Furthermore, for all the described options a two-maneuver disposal is considered to increase the design robustness with respect to uncertainties in maneuver execution: in fact, whenever errors in the first maneuver produce a deviation from the designed trajectory, the second one can be adjusted to include a trajectory correction. On the other hand, this approach increases the disposal complexity, since multiple maneuvers need to be designed and scheduled.

In this work, the disposal design is formulated as a multi-objective optimization problem solved by means of a multi-objective particle swarm optimizer (MOPSO). This allows us not only to minimize the propellant required for the disposal, but also to take into account for other relevant mission aspects, such as the total disposal duration. An additional advantage of this approach is that, for each disposal option, a set of disposal solutions can be provided to the mission operations team for further assessment. Moreover, in this work the problem formulation is more accurate in terms of propellant available at the end of the mission and constraints on maneuver execution. Although Gaia mission is used as the only test case, the proposed design approach can be easily adapted to any LPO mission orbiting either L_1 or L_2 of the Sun–Earth system.

The rest of this paper is organized as follows. A general overview of the dynamical models and perturbations used to predict spacecraft's motion is

3

firstly given, followed by a brief description of the optimization algorithm used to solve the disposal design problems. Section 4 introduces the three disposal options considered and explains the mathematical formulation of the related optimization problems. Finally, specific constraints considered for Gaia mission are introduced in Sec. 5, followed by the results obtained for Earth re-entry, Moon impact, and heliocentric disposal options.

2. Trajectory propagation

An high-fidelity propagation model is required to study the disposal of LPO missions. To this purpose, a restricted $(n+1)$-body problem approximation is adopted, in which the spacecraft is affected by the gravitational attraction of n bodies, but has no gravitational effect on them. Specifically, the full equation of motion in the Solar System including also the relevant relativistic effects is given by

$$
\begin{aligned}
\ddot{\boldsymbol{r}} = &\, G \sum_i \frac{m_i(\boldsymbol{r}_i - \boldsymbol{r})}{r_i^3} \left\{ 1 - \frac{2(\beta + \gamma)}{c^2} G \sum_j \frac{m_j}{r_j} - \frac{2\beta - 1}{c^2} G \sum_{j \neq i} \frac{m_j}{r_{ij}} + \frac{\gamma |\dot{\boldsymbol{r}}|^2}{c^2} \right. \\
&\, + \frac{(1+\gamma)|\dot{\boldsymbol{r}}_i|^2}{c^2} - \frac{2(1+\gamma)}{c^2} \dot{\boldsymbol{r}} \cdot \dot{\boldsymbol{r}}_i - \frac{3}{2c^2} \left[\frac{(\boldsymbol{r} - \boldsymbol{r}_i) \cdot \dot{\boldsymbol{r}}_i}{r_i} \right]^2 + \left. \frac{1}{2c^2} (\boldsymbol{r}_i - \boldsymbol{r}) \cdot \ddot{\boldsymbol{r}}_i \right\} \\
&\, + G \sum_i \frac{m_i}{c^2 r_i} \left\{ \frac{3 + 4\gamma}{2} \ddot{\boldsymbol{r}}_i + \frac{\{[\boldsymbol{r} - \boldsymbol{r}_i] \cdot [(2 + 2\gamma)\dot{\boldsymbol{r}} - (1 + 2\gamma)\dot{\boldsymbol{r}}_i]\}(\dot{\boldsymbol{r}} - \dot{\boldsymbol{r}}_i)}{r_i^2} \right\},
\end{aligned}
\tag{1}
$$

where $\boldsymbol{r}$ is the point of interest, G is the gravitational constant; m_i and $\boldsymbol{r}_i$ are the mass and the Solar System barycentric position of the $i - th$ body or planetary system, respectively; $r_i = |\boldsymbol{r}_i - \boldsymbol{r}|$; c is the speed of light in vacuum; and β and γ are the parameterized post-Newtonian parameters measuring the nonlinearity in superposition of gravity and space curvature produced by unit rest mass (Seidelmann, 2006). In Eq. 1, the positions, velocities, and accelerations of the n bodies are considered as given values, computed from the JPL DE405 ephemeris model. In our integrations n includes the Sun, planets, the Moon, Ceres, Pallas, and Vesta. For planets with moons, with the exception of the Earth, the center of mass of the system is considered. The dynamical model is written in the J2000.0 Ecliptic reference frame and is commonly referred to as Standard Dynamical Model. To avoid ill-posedness of the system, the dynamics are scaled by astronomical unit (AU, 149597870.69 km) and day (day, 86400 s).

To increase the accuracy of the model the perturbation due to Earth oblateness, solar radiation pressure, and drag are also included. The atmospheric drag is considered only when the spacecraft distance from the Earth surface is less than 800 km.

The integration is carried out by means of an Adams-Bashforth-Moulton variable step-order scheme, with an absolute and relative tolerance of 10^{-12}.

3. MOPSO

Population-based optimizers can be easily modified to deal with a vector of objective functions delivering the entire set of Pareto optimal solutions. Furthermore, particle swarm optimization seems particularly suitable for multi-objective optimization mainly because of the high speed of convergence that the algorithm presents for single-objective optimization (Kennedy and Eberhart, 2001). In a multi-objective optimization problem the objective function is a M dimensional vector

$$\boldsymbol{f}(\boldsymbol{x}) = (f_1(\boldsymbol{x}), f_2(\boldsymbol{x}), \ldots, f_M(\boldsymbol{x})). \tag{2}$$

In this frame, a criterion to compare vectors is necessary to identify the optimal solution set. The Pareto dominance is the appropriate criterion to serve this aim, enabling the solutions ranking (Deb, 1999).

The MOPSO implemented for the solution of the problem at hand is based on the following algorithmic flow (Armellin and Lavagna, 2008):

1. Randomly initialize, within the search space, N individuals or particles $\boldsymbol{x}_i$ and set to the same value each personal best solution , i.e. $\boldsymbol{p}_{i,\text{best}} = \boldsymbol{x}_i$

2. Evaluate the objective function

$$\boldsymbol{y}_i = \boldsymbol{f}(\boldsymbol{x}_i) \quad \text{for} \quad i = 1, \ldots, N. \tag{3}$$

3. Update the personal best solution $\boldsymbol{p}_{i,\text{best}}$. The solutions are compared using the Pareto dominance criterion. Thus, for each particle i, with $i = 1, \ldots, N$ we have

$$\boldsymbol{p}_{i,\text{best}} = \begin{cases} \boldsymbol{x}_i & \text{if } \boldsymbol{x}_i \text{ dominates } \boldsymbol{p}_{i,\text{best}} \\ \boldsymbol{p}_{i,\text{best}} & \text{if } \boldsymbol{p}_{i,\text{best}} \text{ dominates } \boldsymbol{x}_i . \\ \boldsymbol{x}_i \text{ or } \boldsymbol{p}_{i,\text{best}} \text{ randomly} & \text{in the other cases} \end{cases} \tag{4}$$

4. Update global best list $\boldsymbol{G}_{\mathrm{best}}$. In the multi-objective problem $\boldsymbol{G}_{\mathrm{best}}$ is the analogous of the scalar global best $\boldsymbol{g}_{\mathrm{best}}$ and it represents the entire set of non-dominated solutions. This list is updated by processing the subset of non-dominated solutions $\boldsymbol{x}_j$ with $j = 1, \ldots, N^* \leq N$

   - If $\boldsymbol{x}_j$ is dominated by one of the solution belonging to the list, do not update the list

   - If $\boldsymbol{x}_j$ dominates one or more solutions belonging to the list, then add $\boldsymbol{x}_j$ to the $\boldsymbol{G}_{\mathrm{best}}$ list and delete the dominated solutions

   - If $\boldsymbol{x}_j$ neither dominates nor is dominated by any solution belonging to the $\boldsymbol{G}_{\mathrm{best}}$ list, then simply add $\boldsymbol{x}_j$ to the list

5. Update the global best solution $\boldsymbol{g}_{\mathrm{best}}$. Note that the $\boldsymbol{g}_{\mathrm{best}}$ is univocally defined for a scalar objective function, whereas it must be opportunely chosen within the $\boldsymbol{G}_{\mathrm{best}}$ list in the multi-objective case. The selection of the $\boldsymbol{g}_{\mathrm{best}}$ plays a key role in obtaining a uniform set of Pareto optimal solutions. For this purpose a uniform 30 cells grid in the objective space is defined at each iteration and the number of solutions belonging to each grid cell is calculated. Based on this number, a roulette-wheel method is then applied to promote the selection of $\boldsymbol{g}_{\mathrm{best}}$ in a low populated grid-cell.

6. Compute the new particles position by

$$\boldsymbol{x}_i^{k+1} = \boldsymbol{x}_i^k + \boldsymbol{v}_i^{k+1}\Delta t \quad \text{for} \quad i = 1, \ldots, N, \tag{5}$$

   in which $\boldsymbol{v}_i^{k+1}$ is the velocity of the i-th particle at the $(k+1)$ iteration, given by

$$\boldsymbol{v}_i^{k+1} = w^k \boldsymbol{v}_i^k + c_1 r_1^k \frac{\boldsymbol{x}_i^k - \boldsymbol{p}_{i,\mathrm{best}}}{\Delta t} + c_2 r_2^k \frac{\boldsymbol{x}_i^k - \boldsymbol{g}_{\mathrm{best}}}{\Delta t}. \tag{6}$$

7. Repeat 2-6 until the convergence criterion is satisfied or the maximum number of iterations is reached.

The parameters c_1 and c_2 of Eq. (6) are considered constant and equal to 2 during the optimization, assuring a balance between local and global terms. A linear decrease of the inertia w with the iteration number in the interval $[0.4, 1.4]$ is adopted. In particular a greater value of the inertia enables a better exploration of the search domain in the first phase of the optimization, whereas a lower value allows a better analysis of the most promising areas of

research space in the subsequent phases. Finally r_1 and r_2 are two random numbers in the range $[-1, 1]$, and Δt is set equal to 1. Note that if the position of a particle goes outside the search space, the violated component of the decision vector takes the value of the corresponding boundary and its velocity component is multiplied by a random number between $[-1, 0]$.

The maximum numbers of particle belonging to the $\boldsymbol{G}_{\mathrm{best}}$ is fixed to 100 units. The same procedure adopted for selecting the $\boldsymbol{g}_{\mathrm{best}}$ is used to delete those solutions belonging to a highly populated grid-cell, if the maximum list size is exceeded.

The convergence criterion adopted is based on the comparison of the average position of the non dominated solutions in the objective space with the same average position of the previous 20 iterations. If the component-wise difference of these two vectors is lower than 1% (or a maximum number of iterations is reached) the Pareto set of optimal solutions is assumed to have been found.

4. Disposal options and their optimization

Three different options for the disposal of LPO missions are considered:

1. Earth re-entry;
2. Lunar impact;
3. Disposal on graveyard orbits.

The approach is very similar for the first two options, although some intrinsic differences remain as, for instance, for what concerns the sustainability constraints. In this sense, different mitigation rules and treaties exist: for the Earth, the requirements on space debris mitigation (ESA, 2008) state that, whenever the total casualty risk is larger than 1×10^{-4}, a controlled re-entry must be performed. In light of the above, five impact regions (the oceans and polar regions) can be defined, such that the casualty risk constraint is always satisfied independently of the spacecraft casualty area (Di Mauro et al., 2013). For what concerns the Moon, the impact should be compliant with all mitigations and treaties related to the lunar environment (UN, 2002); moreover, any interference with the historical heritage sites should be avoided to preserve the historical and scientific value of lunar artifacts placed in these sites (NASA, 2011). Similarly to Earth re-entry, four areas on the lunar surface can be identified for lunar impacts such that these constraints are met (Di Mauro et al., 2013).

In this work, however, the impact with the target is identified by simply measuring the distance between the spacecraft and the body surface, without any constraint on the actual impact point. In light of this consideration, the same approach could be used for the design of disposal trajectories involving Earth re-entry or lunar impact. Therefore, a unified presentation of these two strategies is given in Sec. 4.1. Nonetheless, it is worth highlighting that, once a global solution is available, specific points on the Earth/Moon surface can be easily targeted using a local optimizer, as shown by the authors in Di Mauro et al. (2013).

4.1. Impact with celestial bodies

This disposal strategy is based on designing two impulsive maneuvers to transfer the spacecraft from the LPO to a target celestial body. A first maneuver allows the satellite to leave the LPO, whereas a mid-course maneuver is added to adjust its trajectory to guarantee the impact on the body surface. In addition, the mid-course maneuver is potentially useful to correct possible position/velocity errors deriving from the execution of first maneuver.

The disposal design is formulated as an optimization problem in which the optimization vector is

$$\boldsymbol{x} = (t_d, \Delta V_1, \alpha_1, \delta_1, ToF_1, \Delta V_2, \alpha_2, \delta_2, ToF_2) \tag{7}$$

where t_d is the disposal epoch, ΔV_1 and ΔV_2 are the magnitude of the maneuvers, and ToF_1 and ToF_2 are the transfer times for the two trajectory legs in which the transfer is divided. Polar angles α_1, δ_1, α_2 and δ_2 are used to describe the directions of the first and second maneuver, respectively.

The following constraints on the optimization variables are considered:

1. the disposal maneuver must occur after the mission EoL within a given window;
2. the total time of flight $ToF = ToF_1 + ToF_2$ must be lower than a maximum value set by operations' costs and complexity;
3. the total $\Delta V = \Delta V_1 + \Delta V_2$ must be compatible with the available propellant at EoL;
4. angles $\alpha_i \in [0, 2\pi]$ and $\delta_i \in [-\pi/2, \pi/2]$ are used to compute the maneuver efficiency as described in Sec. 5.1.2.

The optimization of the disposal maneuvers is achieved by defining a dynamic objective function. For the particles that do not reach the target celestial body, the performance index is reduced to the scalar $f(\boldsymbol{x}) = \min d_{S/C-T}$,

where $d_{S/C-T}$ is the distance between the spacecraft and the target at the end of the integration window. For the particles for which the impact is verified, the performance function becomes $\boldsymbol{f}(\boldsymbol{x}) = (ToF, m_p)$, in which m_p is the propellant mass consumption associated to total ΔV.

The problem formulation is summarized in Table 1, in which R_T is the radius of the target body. Note that the objective functions are suitably scaled such that the solutions that satisfy the impact constraint are always Pareto optimal with respect to those that violate it. The optimization problem is solved with the MOPSO using a population of 750 particles and 30 iterations.

Table 1: Problem formulation for the disposal strategies involving the impact with celestial bodies

Condition	Objective function
$\min d_{S/C-T} > R_T$	$f(\boldsymbol{x}) = \min d_{S/C-T}$
$\min d_{S/C-T} < R_T$	$\boldsymbol{f}(\boldsymbol{x}) = (ToF, m_p)$

4.2. Disposal on heliocentric graveyard orbits

Typically, LPO missions can be easily injected into heliocentric orbits, exploiting the inbound or outbound unstable manifold. However, long-term propagations highlight the possibility of spacecraft reentries in the Earth-Moon system, which may lead to potential close encounters with the Earth (Di Mauro et al., 2013). Thus, a disposal strategy is necessary to avoid the long-term occurrence of risky conditions. In this section, two different approaches are proposed. The first is a fully numerical approach based on the solution of a multi-objective optimization problem. The second is based on energetic considerations carried out in the circular restricted 3-body problem (CR3BP).

Both approaches guarantee that heliocentric orbits do not return to Earth's vicinity for at least 100 years from disposal epoch in the high-fidelity dynamical model.

4.2.1. Numerical approach

Within the numerical approach, the computation of heliocentric graveyard orbits is based on a simple definition and solution of a multi-objective optimization problem. One impulsive maneuver is considered, such that the

optimization vector is $\boldsymbol{x} = (t_d, \Delta V, \alpha, \delta)$. The same constraints introduced in Sec. 4.1 are applied to the optimization variables.

The optimization of the disposal maneuvers is achieved by defining again a dynamic objective function. For particles that get closer to the Earth than 0.05 AU (distance typically used to classify celestial bodies as potentially hazardous objects) the performance index is reduced to the scalar $f(\boldsymbol{x}) = -\min d_{S/C-E}$, where $d_{S/C-E}$ is the minimum distance reached by the spacecraft with respect to the Earth in the propagation window. For particles whose trajectories do not enter the 0.05 AU sphere around the Earth, $\boldsymbol{f}(\boldsymbol{x}) = (m_p, -\min d_{S/C-E})$.

The problem formulation is summarized in Table 2, in which R_T is the radius of the target body. Note that the objective functions are suitably scaled so that trajectories that do not enter the 0.05 AU sphere around the Earth always dominate those that violate this constraint. The optimization problem is solved with the MOPSO using a population of 35 particles and 20 iterations.

Table 2: Problem formulation for the disposal on graveyard orbits using the numerical approach.

Condition	Objective function
$\min d_{S/C-E} < 0.05$ AU	$f(\boldsymbol{x}) = -\min d_{S/C-E}$
$\min d_{S/C-T} > 0.05$ AU	$\boldsymbol{f}(\boldsymbol{x}) = (m_p, -\min d_{S/C-E})$

4.2.2. Energetic approach

An alternative approach for the identification of heliocentric graveyard orbits for LPO entails energetic considerations. Let us consider a spacecraft orbiting around L_2. A qualitative analysis of its motion and the associated energy levels can be captured by a simple CR3BP, where the Sun and the Earth+Moon system represent the two primaries. The use of this dynamical model eases the identification of the main conditions to obtain heliocentric graveyard orbits, which are the starting point for the following analysis.

With reference to Fig. 1, the energy level associated to the L_2-LPO allows the spacecraft to travel in the exterior region, the Earth+Moon region, and the interior region of the system (the grey area corresponds to the forbidden region, also referred to as Hill's region; the white area is the admissible region).
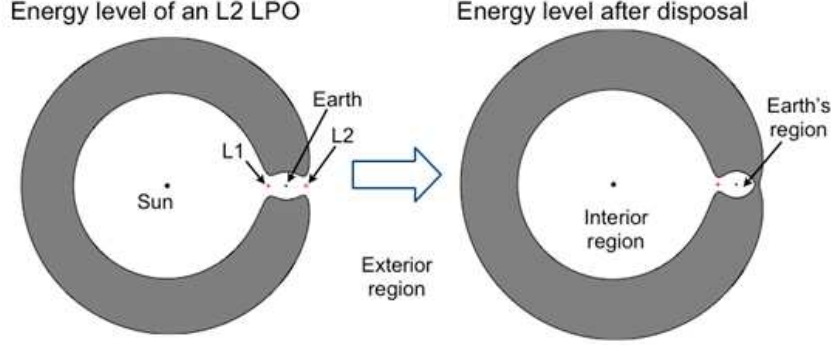
10

Figure 1: Heliocentric graveyard orbit definition based on the energetic approach.

Roughly speaking, a disposal maneuver can be suitably designed to reduce the energy level of the spacecraft when it is moving in the exterior region such that the forbidden region closes at L_2. In this way, the spacecraft is permanently confined to a region beyond Earth's orbit and no longer represents a potential hazard for Earth's assets. The same technique can be applied to spacecraft moving the interior region with the difference that, in this case, the energy level must be reduced such that the Hill's region closes at L_1.

More in detail, the CR3BP possesses an integral of motion, the so-called Jacobi constant, defined in Szebehely's coordinates (Szebehely, 1967) as

$$J(x, y, z, \dot{x}, \dot{y}, \dot{z}) = 2\Omega(x, y, z) - (\dot{x}^2 + \dot{y}^2 + \dot{z}^2), \tag{8}$$

where

$$\Omega(x, y, z) = \frac{1}{2}(x^2 + y^2) + \frac{1-\mu}{r_1} + \frac{\mu}{r_2} + \frac{1}{2}\mu(1-\mu). \tag{9}$$

The parameter μ is the mass parameter ($\mu = 3.0404 \ 10^{-6}$ for Sun-Earth system), whereas r_1 and r_2 are the distances of the third body from the primaries, located at $x = -\mu$ and $x = 1 - \mu$. This integral is strictly related to mechanical energy of the system by the relation

$$J = -2E, \tag{10}$$

meaning that high values of J are associated to low energy levels. Thus, reducing the energy level is equivalent to increasing the Jacobi constant.

Indeed, the forbidden region can be closed by properly increasing the Jacobi constant. More specifically, if

$$J > J_{L_2}, \tag{11}$$

where J_{L_2} indicates the value of the Jacobi constant at L_2, the region closes at L_2 and the motion of the spacecraft can be confined to the outer region, beyond Earth's orbit.

Based on this consideration, let us now consider a tangential maneuver such that the spacecraft velocity, v', is given by

$$v' = v + \Delta V. \tag{12}$$

This yields

$$J' = 2\Omega - v'^2. \tag{13}$$

Subtracting Eq.(13) by Eq. (8) and rearranging terms yield an expression that links the value of ΔV to the variation of the Jacobi constant ΔJ

$$\Delta V = -v \pm \sqrt{v^2 - \Delta J}. \tag{14}$$

Typically the roots corresponding to the minus sign are discarded since they refer to retrograde orbits. Therefore, by assuming $J' > J_{L_2}$ (such that the Hill's region closes at L_2), the corresponding ΔV can be easily found from Eq. (14). Analogous considerations hold for heliocentric graveyard orbits in the interior region. In this case, however, the value of J should be raised above J_{L_1} to avoid reentries, as the forbidden region shall be closed at L_1.

The main drawback of this energetic approach lies in its complexity when the $(n + 1)$-body problem, including solar radiation pressure, is considered. In this dynamical model, J is no more constant due to the gravitational perturbations of other bodies, the eccentricity of primaries' orbits, and the solar radiation pressure. Thus, the value of J varies along the trajectory and several oscillations, above and below the threshold J_{L_2}, can be observed (see Fig. 2). This leads to the sequential opening and closure of Hill's curves, which makes predicting the occurrence of spacecraft re-entry in the Earth-Moon system very difficult.

In light of these considerations, the goal of the proposed energetic approach is to determine the minimum value of ΔJ that is necessary to guarantee that Eq. (11) is always satisfied in the high-fidelity model for at least
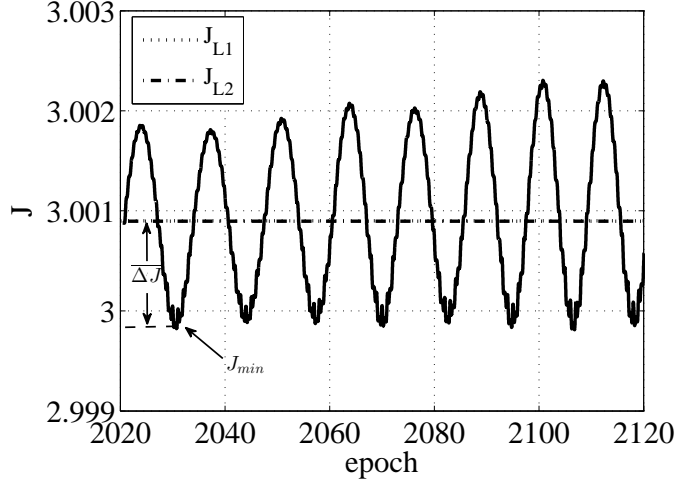
12

Figure 2: Example of the Jacobi integral profile in a $(n+1)$-body model.

100 years from the disposal epoch. This condition might seem unnecessary since, to avoid re-entries in the Earth-Moon system, it is sufficient to ensure that J is larger than J_{L_2} only when the spacecraft is actually close to the Earth-Moon system. On the other hand, this logic allows one to obtain more robust solutions, since a safety margin on J is guaranteed whenever the spacecraft has a close approach with the Earth-Moon system. Moreover, within this approach the disposal solutions are likely to be valid for intervals longer than the designed 100 years.

A first option is to set ΔJ equal to the maximum variation of J experienced in the first 100 years of natural spacecraft motion (see Fig. 2), given by

$$\overline{\Delta J} = J_{L_2} - J_{min}. \tag{15}$$

However, this value may turn out to be so large that the corresponding ΔV, computed by Eq. (14), exceeds the available resources. The introduction of a small maneuver to move the spacecraft to a suitable exterior trajectory has shown to reduce the required ΔJ and, more in general the overall disposal ΔV. For this reason, despite the increasing of the disposal complexity, an initial maneuver has been included in the design process. As a result, differently from the numerical approach, the energetic one consists in a two-maneuver disposal: the first one allows the spacecraft to properly

13

leave the nominal LPO and to reach the exterior region, whereas the second one guarantees the closure of Hill's regions, avoiding possible re-entry in the Earth-Moon system. It is worth remarking that, as long as the satellite is on the nominal LPO, the corresponding Hill's regions must be open at that libration point L_i. The closure of the Hill's curves (i.e., raising J above the threshold value J_{L_i}) is possible only when the spacecraft is in the interior/exterior region. This explains why a second disposal maneuver is necessary.

The design of heliocentric graveyard orbits based on the energetic approach goes through a three-step optimization process:

1. *First maneuver optimization.* The computation of the first maneuver is performed through a multi-objective optimization on the set of parameters

$$\boldsymbol{x} = (t_d, \Delta V_1, \alpha_1, \beta_1), \qquad (16)$$

for which the same constraints introduced in Sec. 4.1 are applied. The goal is to identify the initial maneuver that maximizes the minimum value of the Jacobi constant over a 100 years window, i.e. $\boldsymbol{f}(\boldsymbol{x}) = (m_p, -\min(J))$.

2. *Second maneuver design.* The second maneuver is assumed tangential to the spacecraft velocity, and thus the set of unknowns reduces to the maneuver magnitude ΔV_2 and the epoch, defined by $t_d + ToF_1$. Since the aim is to close Hill's region at L_2, the first guess for ΔV_2 is computed using Eq. (14) and (15). It is worth highlighting that, as the minimum value of J is increased by executing the first maneuver, the ΔJ required to close Hill's region with the second maneuver and the associated ΔV_2 are significantly reduced.

However, the value of ΔV_2 is not only defined by ΔJ, as it depends on the spacecraft velocity in the rotating frame and, thus, on the epoch at which the maneuver is executed. An analysis of the trend of ΔV_2 with respect to the epoch is carried out (an example is reported in Fig. 3). The values of ΔV_2 are negative, which means the maneuver must be oriented in the opposite direction with respect to the spacecraft velocity. In addition, it is worth observing that the maneuver turns out to be unfeasible at some epochs, since the presence of the square root in Eq. (14) leads to complex solutions whenever the value of ΔJ is larger than the maximum variation allowed at that epoch ($\Delta J_{max} = v^2$). In
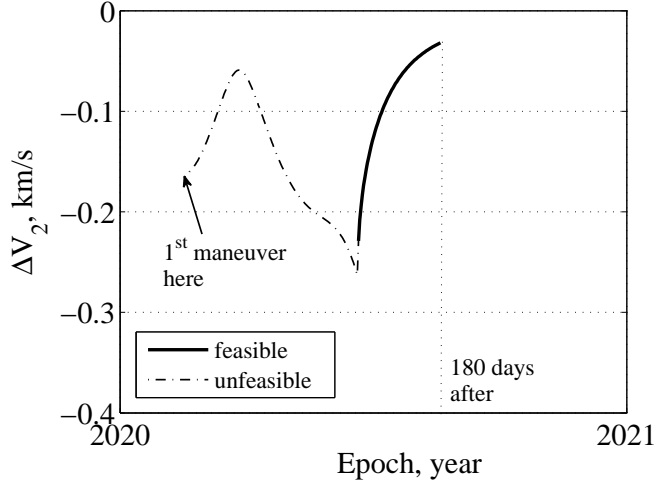
14

Figure 3: ΔV_2 profile for a fixed value of ΔJ.

particular, the larger ΔJ is, the greater is the set of unfeasible solutions. In the worst case, feasible solutions are available only after a long time (greater than the maximum disposal duration) and the method fails. In these cases two alternatives are available: a) relaxing the constraint on the maximum disposal duration or b) closing the curves only when the spacecraft has a close approach with the Earth-Moon system, thus reducing the required ΔJ.

Since the aim is to reduce the maneuver cost, an obvious choice is to perform this second maneuver at the epoch at which the resulting ΔV_2 is minimum. This condition is typically achieved at the apocenter/pericenter of the heliocentric orbit, depending if the spacecraft is moving toward the exterior or interior region, respectively. However, the required waiting time typically leads to a violation of the constraint on the maximum disposal duration. Therefore, earlier epochs are chosen at the cost of a larger ΔV_2.

3. *Second maneuver optimization.* The last step involves the use of a bisection method to refine the value of ΔV_2 so that Hill's region remain closed for at least 100 years in the high-fidelity dynamical model. After the application of the ΔV_2 computed in the CR3BP, Hill's region may still be open in the high-fidelity model or $\min J$ may be larger that J_{L_2}. Therefore, a bisection algorithm is exploited to find the ΔV_2 that

15

solves

$$\min J - J_{L_2} = 0, \tag{17}$$

where $\min J$ is computed on the 100-year window. Equation 17 ensures that the Jacobi constant is always above J_{L_2}, thus precluding any possible reopening of the forbidden region.

5. The case of Gaia

Gaia is an ESA mission, successfully launched in December 2013, with the aim of building the most precise 3D map of the Milky Way and answer questions about its origin and evolution. This ambitious goal will be achieved through the survey of one thousand million (one billion) stars in our galaxy and local galactic neighborhood. This search has also some secondary effects, since it will enhance the probability to discover planets beyond our Solar System and asteroids and comets within it. The mission will also reveal tens of thousands of failed stars and supernovae, and will even test Einstein's famous theory of General Relativity. All these goals will be achieved thanks to an intense activity that will nominally last until July 2019. In this section we show the results obtained for Gaia disposal using the three different strategies presented in the previous section.

5.1. Problem definition

This section briefly describes the computation of Gaia's initial conditions (state vector and available propellant mass) for the entire EoL disposal window.

We use 12 May 2014 as the reference initial epoch t_0 and indicate the corresponding initial position and velocity with $\boldsymbol{r}_0$ and $\boldsymbol{v}_0$, respectively. Besides the initial conditions, the area-to-mass ratio A/m is needed to propagate the dynamics in the high-fidelity model. A first estimate of A/m can be obtained by using the nominal values of A and m, and considering the Sun-aspect angle of Gaia fixed at 45 deg to keep the thermal balance (Renk and Landgraf, 2014). However, a more accurate can be estimated in the following way. Starting with the first estimate of A/m provided above, the dynamics is propagated from t_0 to the nominal EoL epoch t_{EoL}, which has been set to 30 Jun 2019. The value of A/m is then recursively adjusted to obtain the trajectory that remains in the operative region for the longest window.

16

In this way, an average value of 0.0196 m^2/kg is obtained. The dynamics is, therefore, propagated from t_{EoL} to the end of the disposal window, $t_{\overline{EoL}}$, fixed at 31 December 2020.

Some station-keeping maneuvers are also included in the propagation process, with a period of about 3 months. As suggested by Hechler et al. (2002), these maneuvers are computed in the algorithm as small velocity corrections ($\approx$ cm/s) along $\boldsymbol{u}$, that is the escape direction in the linear theory (28.6 degrees with respect to the x-axis). The results of these propagations are shown in Fig. 4.
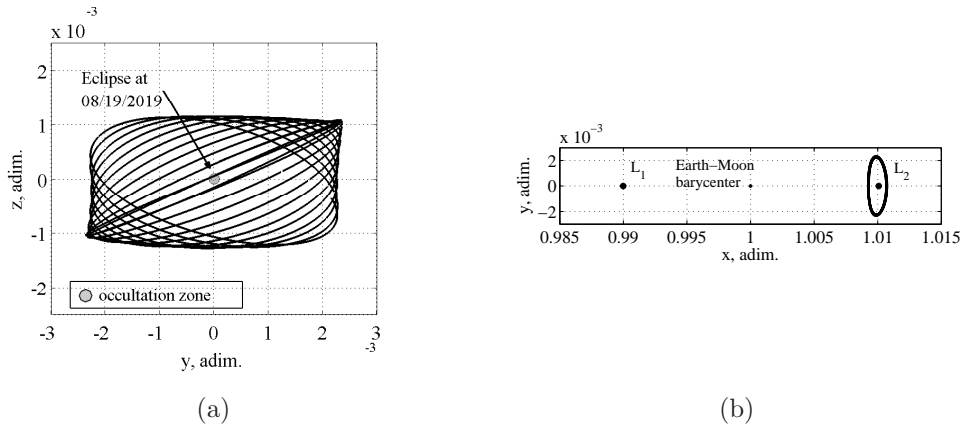
Figure 4: Propagation of Gaia motion from t_0 to $t_{\overline{EoL}}$. (a) y, z view (The gray circle illustrates the occultation zone produced by Earth); (b) x, y view.

As expected, Gaia will experience an eclipse in the middle of August 2019, just after the nominal end of the mission epoch. An eclipse avoidance maneuver is therefore necessary, since Earth's shadow could produce occultations of the Sun, that means the spacecraft could be unable to obtain solar energy. To this purpose, different techniques for the generation of an artificial exclusion zone are available: the first one is the LOEWE (Lissajous Orbit Ever Without Eclipse) strategy (Canalias et al., 2003); the second one uses instead the idea of phase synchronization as introduced by Farquhar (1971).

Since Gaia shall be operated longer, the phase synchronization option is discarded and the LOEWE strategy is selected. This technique is firstly applied to the linearized solution of the CR3BP. The results are then used as an initial guess for the algorithm calculating the occultation or eclipse avoidance maneuvers in the full model $((n+1)$-body + SRP).

17

5.1.1. LOEWE eclipse avoidance maneuver

A brief description of the LOEWE eclipse avoidance maneuver is reported in this section. The reader is referred to Canalias et al. (2003) for an exhaustive explanation of all the steps required for its computation. Firstly, we introduce the effective phases, defined as

$$\Phi = \omega t + \phi; \qquad \text{in-plane} \tag{18}$$

$$\Psi = \nu t + \psi. \qquad \text{out-of-plane} \tag{19}$$

where ω and ν are the in-plane and out-of-plane frequencies, t is the time and ϕ and ψ are the initial phases, for in-plane and out-of-plane motion, respectively. The exclusion zone generation is reduced to a simple geometrical problem, independent of the epoch. The basic idea of the LOEWE strategy is to perform a phase jump (either an in-plane jump, within the x, y plane, or an out-of-plane jump, along z direction), just prior to the trajectory entering the exclusion zone. The magnitude of the phase jump is exactly as big as required for the resulting trajectory to be tangent in the Effective Phase Plane (EPP) to the exclusion zone (for which a radius of about 14000 km is typically considered for a mission in the Sun-Earth L_2).

Figure 5 reports both the in-plane and the out-of-plane phase jumps computed for the linearized solution of the CR3BP.
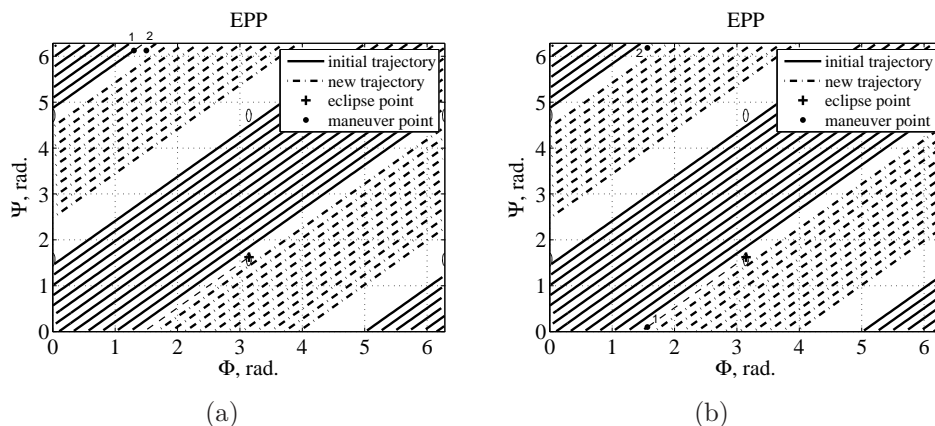

Figure 5: Representation of the eclipse avoidance maneuver in the EPP: (a) in-plane phase jump; (b) out-of-plane phase jump. In both cases, the jump occurs from point 1 to point 2 and leads to the same lower tangential trajectory.

18

It turns out that a jump in z direction, that is a variation in the value of Ψ, is cheaper ($\Delta V = 7.89$ m/s) with respect to a change in the effective phase Φ, within the xy plane ($\Delta V = 26.24$ m/s). The choice among them is driven by the amount of propellant required, thus the out-of-plane maneuver is selected. This value is used as first guess in a local constrained optimization, through which the maneuver is refined for the full model. As illustrated in Figure 6, the new trajectory is always out of the exclusion zone thanks to a $\Delta \dot{z}$ of about 11 m/s. It is interesting to note that the maneuver is scheduled for July 5 2019, just few days after the nominal end of the mission.

$$(a) \qquad\qquad\qquad\qquad (b)$$
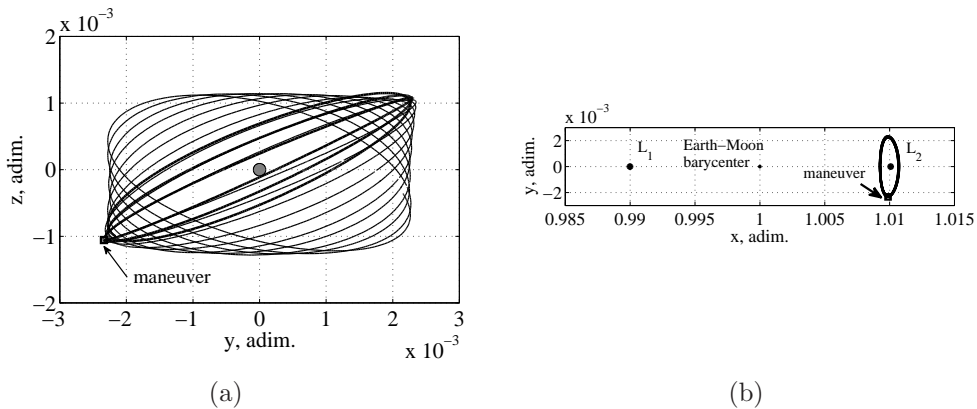
Figure 6: Propagation of Gaia motion from t_0 to $t_{\overline{EoL}}$ after the LOEWE maneuver. (a) y,z view (The gray circle illustrates the occultation zone produced by Earth); (b) x,y view.

5.1.2. Disposal design constraints

Three major constraints are set for the design of Gaia disposal:

1. the disposal shall last maximum 180 days;
2. the disposal shall be performed in the interval from 1 July 2019 to 31 December 2020;
3. the available ΔV depends on the maneuver direction.

The first two constraints are set by ESA and are mainly driven by operation costs and complexity considerations. The third constraint is associated to Gaia system design. In fact, as explained by Renk and Landgraf (2014), the thrusters on Gaia have different geometric efficiencies (indicated with η in the remainder of the paper) based on maneuver direction. In particular,

for any maneuver after the science phase, the following efficiency plot needs to be considered
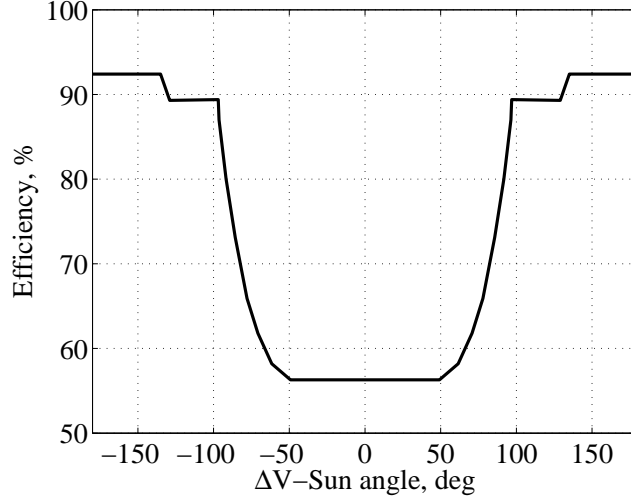

Figure 7: Maneuver efficiency dependant on ΔV–Sun angle for Gaia.

Knowing the angle with respect to the Sun for a certain maneuver (available from α_i and δ_i), the corresponding value of the geometric efficiency is easily obtained.

5.1.3. Available propellant

The last missing piece for the definition of Gaia disposal problem is the estimation of the available propellant mass. From the latest estimations, about 115 kg of propellant will be left after the eclipse avoidance maneuver. This means a nominal ΔV of about 218.75 m/s, since Gaia dry mass is about 1392 kg, and its main propulsion system has a specific impulse of 281 s. Combining these information with geometric efficiency of Fig. 7, and eclipse avoidance and station keeping maneuvers directions, the propellant mass available for the entire disposal window can be computed. The obtained profile of the available propellant mass is reported in Fig. 8.

Thus, at any given disposal epoch t_d, the available propellant can be computed, together with the spacecraft state obtained with the high-fidelity propagation. The entire list of the computed maneuvers (LOEWE + station keeping) is reported in Table 3, where ΔV^* is the value of ΔV taking into account maneuver efficiency. Note that the implemented sequence of
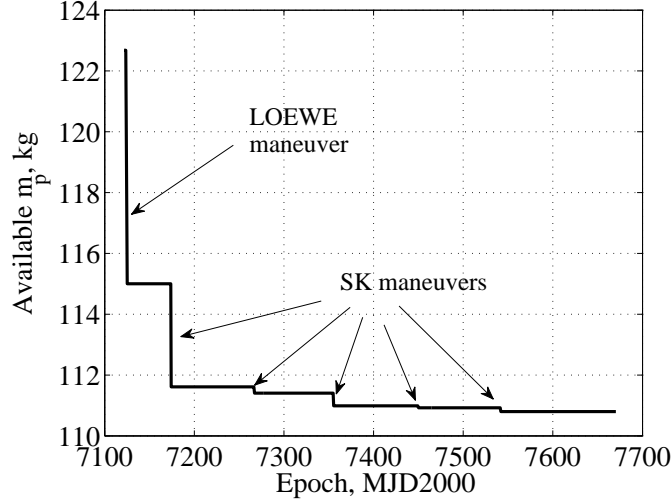
20

Figure 8: Propellant mass availability for Gaia as a function of the epoch.

station-keeping maneuvers is only an approximation required to estimate the propellant available at EoL. The actual ΔV cannot be predicted at this stage of the mission, since they depend on many factors such as the accuracy of orbit determination, the execution accuracy of previous station-keeping maneuvers, degradation of spacecraft optical properties.

Table 3: List of maneuvers for Gaia.

ΔV^* (ΔV)	Epoch	ΔV–Sun angle	Efficiency
m/s	mjd2000	deg	%
14.082 (10.99)	7125.219	90.060	0.7811
6.239 (3.513)	7174.173	28.587	0.5630
0.374 (0.346)	7267.240	151.370	0.9240
0.773 (0.435)	7355.436	28.563	0.5630
0.115 (0.106)	7450.142	151.343	0.9240
0.232 (0.131)	7541.938	28.539	0.5630

5.2. Earth re-entry

The disposal options identified for the Earth re-entry strategy are presented in this section. The search space for the disposal epoch, t_d, is divided

21

in the three sub-windows

- from 1 Jul 2019 to 31 Dec 2019;

- from 1 Jan 2020 to 31 May 2020;

- from 1 Jun 2020 to 31 Dec 2020;

The multi-objective optimization problem is solved in each sub-window. The whole set of feasible solutions (i.e., satisfying the constraint min $d_{S/C-E} < R_E$) is reported on the left in Fig. 9–11 where the Pareto front is also highlighted. In addition, for each sub-window, a solution from the Pareto front is selected: the associated trajectory is reported on the right in the same figures, whereas the details of the resulting disposal maneuvers are summarized in Table 4.

Figure 9(a) reports the solutions in the interval from 1 Jul 2019 to 31 Dec 2019. From the resulting Pareto front, a disposal strategy characterized by a total propellant consumption of about 73.59 kg ($\Delta V = 138.28$ m/s) and a total time of flight of about 144.77 days is selected and the resulting trajectory is reported in Fig. 9(b). Note that in order to limit the operational complexity of the disposal, close approaches with the Moon are avoided by discarding all the solutions with a minimum distance from the Moon smaller than 70000 km. The selected solution has a minimum distance from the Moon of about 1.26×10^5 km.

The results obtained in the second sub-window are reported in Fig. 10. In this case, a solution with a total propellant consumption of about 47.53 kg ($\Delta V = 88.56$ m/s) and a total time of flight of about 165.61 days is chosen. The minimum distance from the Moon during the disposal is about 1.00×10^5 km.

Finally, the optimal solutions for the last sub-window are presented in Fig. 11. As can be seen, the set of solutions is relatively small due to the lower availability of propellant for the disposal. This suggests that Earth re-entry is less convenient when it is performed towards the end of the disposal window, and other strategies shall be preferred in this case. For the sake of completeness, one solution is selected from the Pareto front, which is characterized by a total propellant consumption of about 94.89 kg and a time of flight of about 153.53 days. Again, the spacecraft is outside the sphere of influence of the Moon, with a minimum distance of 1.44×10^5 km.
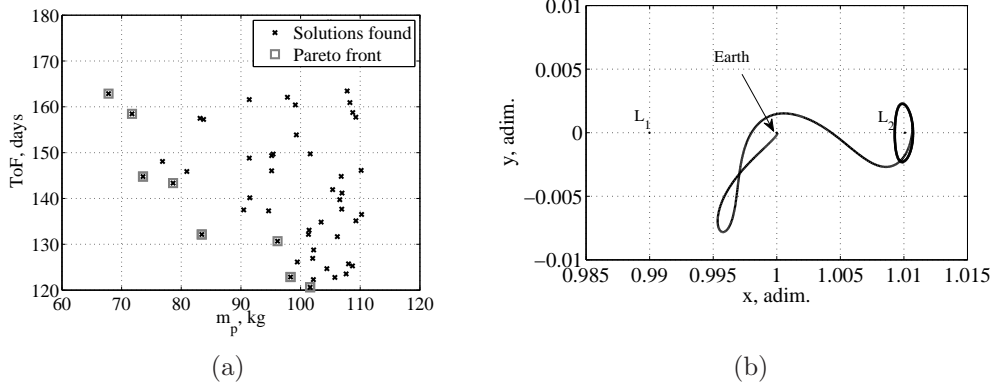
22

Figure 9: Earth re-entry disposal in the interval from 1 Jul 2019 to 31 Dec 2020: (a) Optimal solutions and Pareto front; (b) Trajectory visualization in the synodic frame.

Table 4: Details of the Earth re-entry disposal maneuvers selected for Gaia.

Epoch	2019/11/8 20:37:04.15	2020/4/20 14:13:03.65	2020/6/14 03:55:39.72	UTC
ΔV_1^* (ΔV_1)	137.60 (95.17)	73.01 (49.33)	177.80 (108.41)	m/s
ΔV_1–Sun angle	81.44	79.71	68.61	deg
η_1	69.16	67.57	60.97	%
ΔV_2^* (ΔV_2)	0.68 (0.45)	15.55 (13.26)	1.94 (1.35)	m/s
ΔV_2–Sun angle	78.94	95.23	81.83	deg
η_2	66.86	85.26	69.53	%
m_p	73.59	47.53	94.89	kg
ToF	144.77	165.61	153.53	day

5.3. Lunar impact

The results for the lunar impact disposal are presented in an analogous way. Fig. 12 presents the results for the first disposal window. Fig. 12(b) reports the trajectory of a solution that requires about 37.37 kg of propellant and a total time of flight of about 173.28 days. Note that, for the lunar impact case, the solutions are considered feasible only if the associated trajectory has a minimum distance from the Earth greater than 1×10^5 km. For the solution
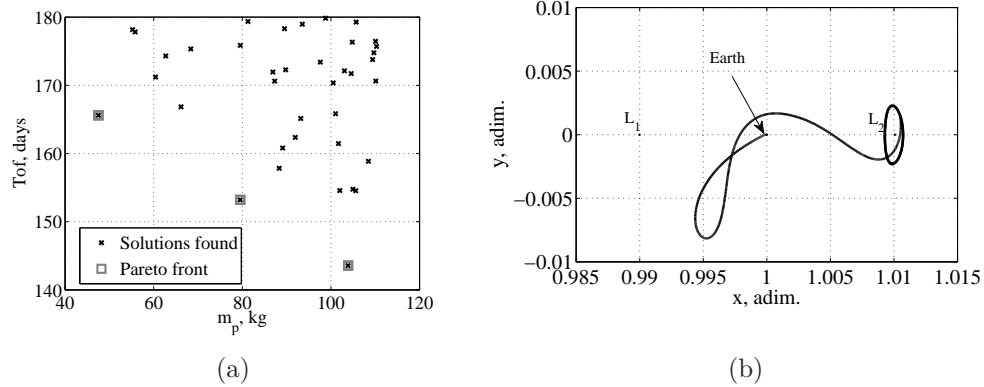
Figure 10: Earth re-entry disposal strategy in the interval from 1 Jan 2020 to 31 May 2020: (a) Optimal solutions and Pareto front; (b) Trajectory visualization in the synodic frame.
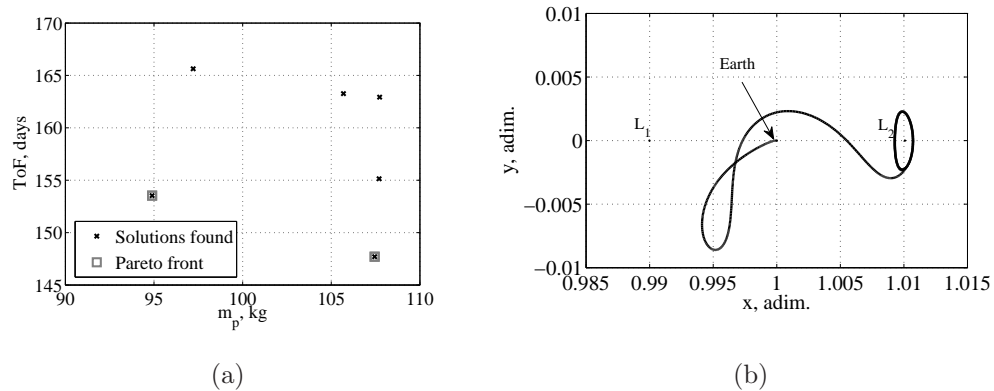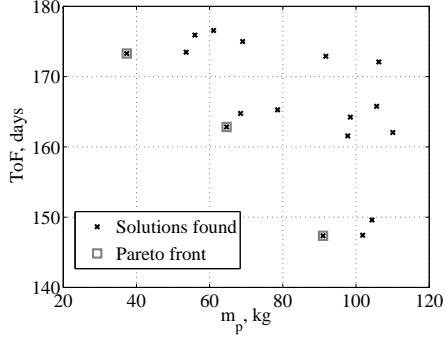

Figure 11: Earth re-entry disposal strategy in the interval from 1 Jun 2020 to 31 Dec 2020: (a) Optimal solutions and Pareto front; (b) Trajectory visualization in the synodic frame.

presented in Fig. 12(b), the minimum distance is 3.93×10^5 km.

The results obtained in the second sub-interval are depicted in Fig. 13. The optimal solution selected, whose trajectory is illustrated in Fig. 13(b), has a total propellant consumption of about 84.65 kg, whereas its impact occurs about 125.57 days after the initial disposal epoch. During disposal, the minimum distance from the Earth is 3.92×10^5 km.

Finally, the solutions set found in the last interval of the disposal window

24
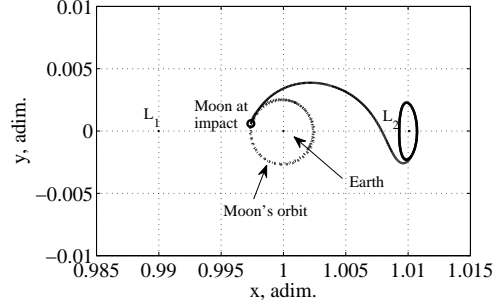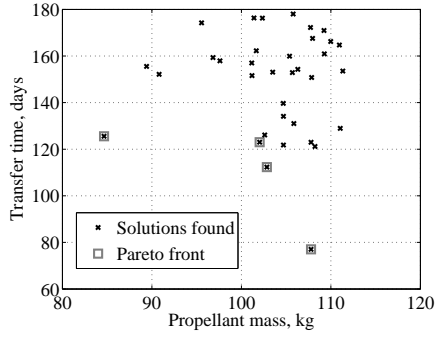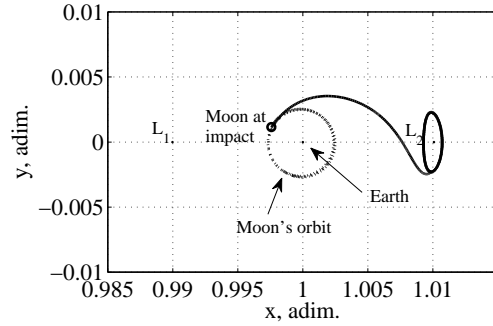
Figure 12: Lunar impact disposal strategy in the interval from 1 Jul 2019 to 1 Jan 2020: (a) Optimal solutions and Pareto front; (b) Trajectory visualization in the synodic frame.

Figure 13: Lunar impact disposal strategy in the interval from 1 Jan 2020 to 1 Jun 2020: (a) Optimal solutions and Pareto front; (b) Trajectory visualization in the synodic frame.

is reported in Fig. 14. The trajectory of the solution with a propellant requirement of about 48.10 kg and a disposal duration of about 144.15 days is plotted in 14(b).The minimum distance from the Earth is 3.69×10^5 km.

The results obtained for lunar impact strategy are summarized in Table 5. Early disposals (within the first sub-window) seem to be preferable, since higher maneuver efficiencies can be obtained.
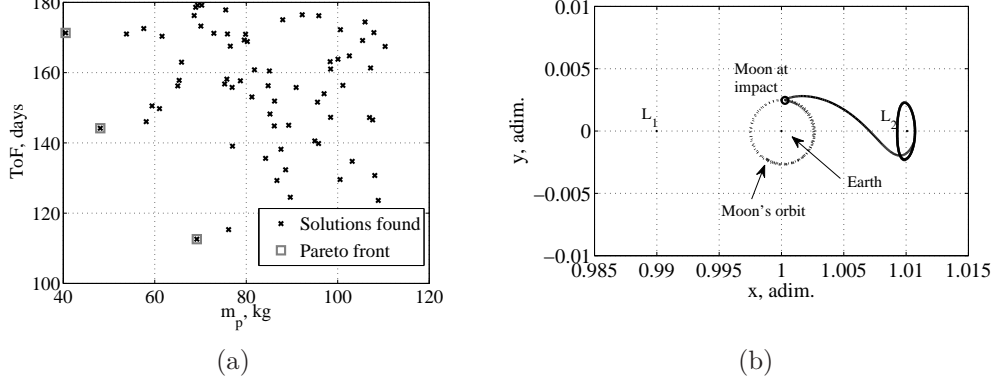
25

Figure 14: Lunar impact disposal strategy in the interval from 1 Jun 2020 to 31 Dec 2020: (a) Optimal solutions and Pareto front; (b) Trajectory visualization in the synodic frame.

Table 5: Summary of the lunar impact options selected for Gaia.

	2019/12/17	2020/01/01	2020/11/19	
Epoch	07:43:16.08	13:37:42.17	17:52:54.76	UTC
ΔV_1^* (ΔV_1)	50.08 (33.92)	90.79 (62.16)	74.85 (42.14)	m/s
ΔV_1t–Sun angle	79.88	80.68	40.15	deg
η_1	67.73	68.47	56.3	%
ΔV_2^* (ΔV_2)	19.28 (17.23)	68.91 (53.12)	14.80 (13.23)	m/s
ΔV_2–Sun angle	115.84	89.16	102.72	deg
η_2	89.34	77.08	89.38	%
m_p	37.37	84.65	48.10	kg
ToF	173.28	125.57	144.15	days

5.4. Heliocentric graveyard orbits

5.4.1. Numerical approach

The heliocentric graveyard orbits obtained for Gaia using the numerical approach are presented in this section. For each disposal sub-window, the whole set of computed potential solutions is first reported. Then, more details are provided for a single solution selected from the Pareto-optimal set.

Figure 15 reports the set of solutions obtained for the interval from 1 Jul

2019 to 31 Dec 2019. It is apparent that a large set of efficient solutions (propellant consumption of the order of 1 kg) are available. These solutions basically consist in a phase-shift between the spacecraft and the Earth, thus allowing the maintenance of a safe distance for a long time window. Also note that increasing the propellant consumption, within the available limits, does not produce better solutions in terms of minimum distance from the Earth.

One solution is selected from the Pareto set: its trajectory and the associated profiles of distance from the Earth and Jacobi integral are reported in Fig. 15(b)–15(d). This solution is characterized by a propellant consumption of only 0.29 kg and a minimum distance from the Earth of 0.06186 AU $(9.25 \times 10^6$ km). Note that from the Jacobi integral plot, the Earth-Moon region is almost always accessible by the spacecraft from an energetic perspective.

Similarly, Fig. 16 reports the solutions found in the second disposal window. The same considerations of the previous disposal window hold. This translates in a Pareto set of two solutions only. Details of the solution, characterized by a propellant consumption of about 1.19×10^{-3} kg and a minimum distance from the Earth of 0.06146 AU $(9.194 \times 10^6$ km), are provided in Fig. 16(b)–16(d). In contrast with the previous case the graveyard orbit is internal to the Earth-Moon system. This is obtained by exploiting a heteroclinic connection that reduces the maneuver ΔV to mm/s level.

The main drawback of the solution is that spacecraft experiences a close passage with the Earth with minimum distance $\approx 1.37 \times 10^5$ km. Figure 17 compares the disposal option with the natural motion of the spacecraft. It is clear that the natural motion leads Gaia towards the Earth-Moon barycenter, where interactions with protected regions or even an uncontrolled impact with our planet can occur. This further supports our claim on the need of planning, designing, and implementing a disposal maneuver. On the other hand, from the same figure it seems that the spacecraft natural motion could be exploited to obtain Earth re-entry or Moon impact disposal options cheaper than those presented in Sec. 5.2 and 5.3. This is true only if the constraint on total disposal duration of 180 days is removed (almost zero cost solutions can be obtained with disposal time greater than 1 year).

The results in the third window are plotted in Fig. 18. The figure reports also the details for a solution with propellant mass consumption of about 0.16 kg and minimum distance from the Earth of 0.06663 AU $(9.97 \times 10^6$ km). Even in this case, Gaia performs a close passage around the Earth
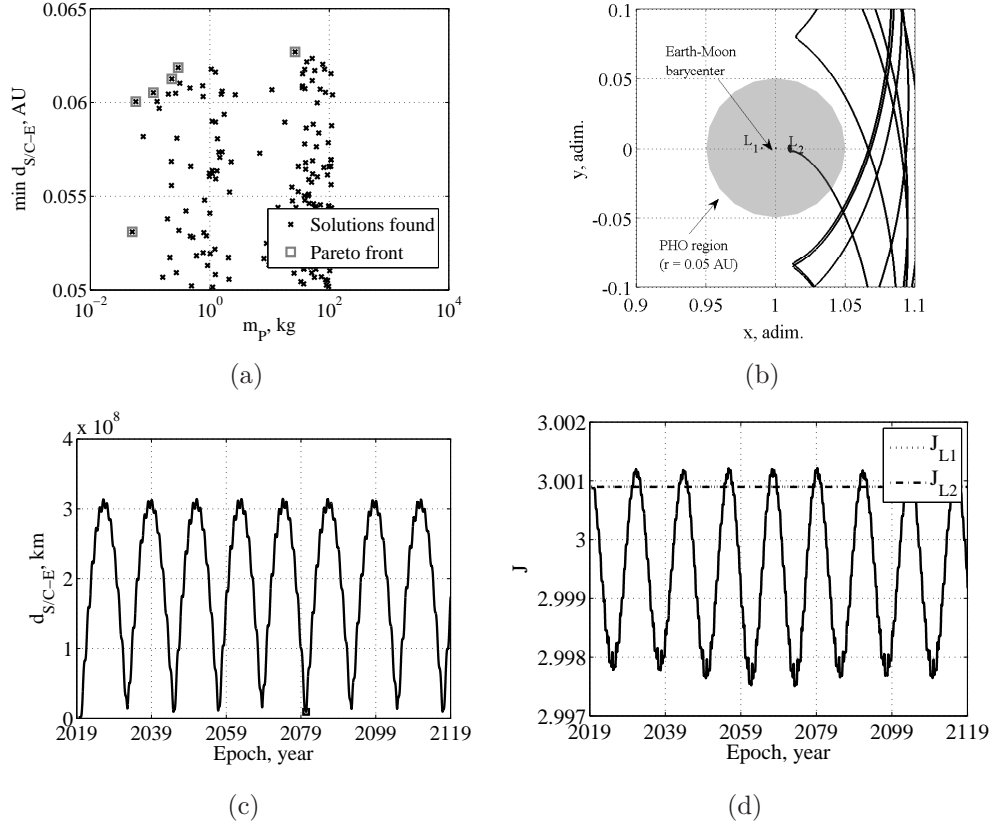
Figure 15: Heliocentric graveyard orbits computed with the numerical approach in the interval from 1 Jul 2019 to 31 Dec 2019: (a) Optimal solutions and Pareto front; (b) Trajectory visualization in the synodic frame; (c) Distance from the Earth (the square highlights the minimum); (d) Jacobi integral profile.

($\approx 10^5$ km) before departing towards the exterior region.

The results obtained for the solutions selected in each sub-window are summarized in Table 6.

It is evident that the numerical approach allows the design of graveyard disposals with limited amount of propellant. On the other hand, the potentially high sensitivity to both maneuver and modelling errors can represent a main limitation to the practical implementation of this approach.
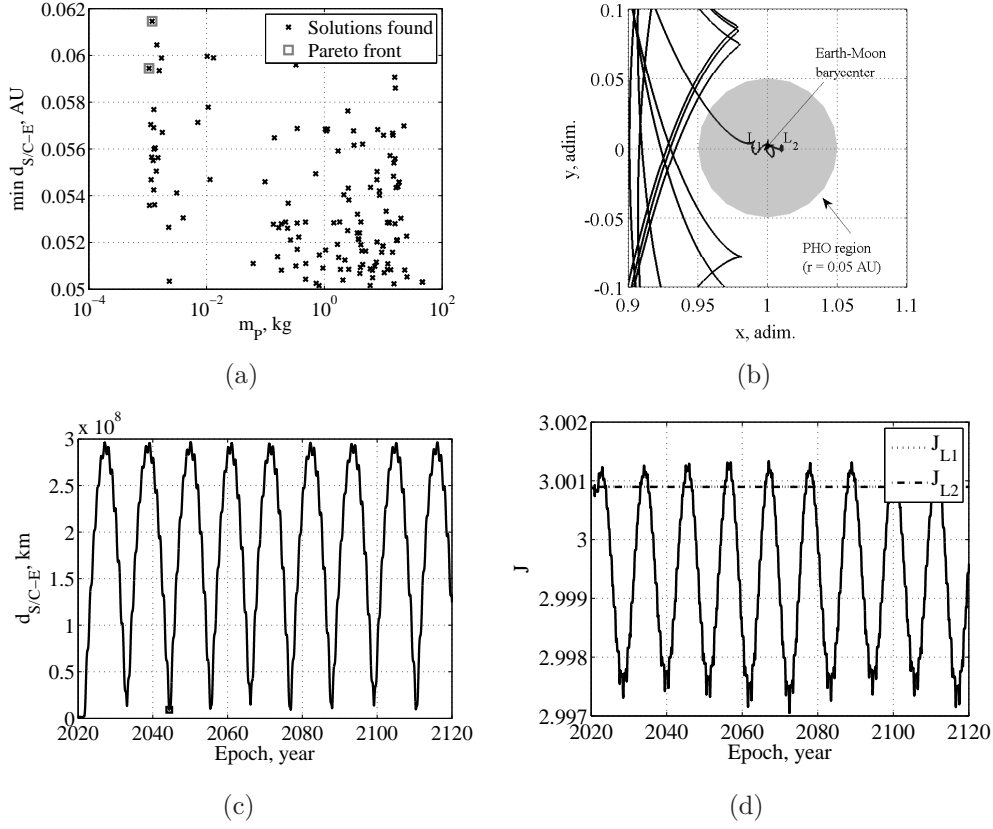
28

Figure 16: Heliocentric graveyard orbits computed with the numerical approach in the interval from 1 Jan 2020 to 31 May 2020: (a) Optimal solutions and Pareto front; (b) Trajectory visualization in the synodic frame; (c) Distance from the Earth(the square highlights the minimum); (d) Jacobi integral profile.

5.4.2. Energetic approach

This section focuses on the heliocentric graveyard orbits obtained using the energetic approach. As anticipated in Sec. 4, this approach does not always produce a valid solution, since the required variation of the Jacobi integral may be larger than the one achievable with the on-board propellant. In fact, this condition is verified in the first and the last sub-windows. Feasible solutions are identified instead in the interval from 1 Jan 2020 to 31 May 2020 and are reported in Fig. 19. Additional information about the plotted solution are also summarized in Table 7, along with details on the maneuvers to be performed.
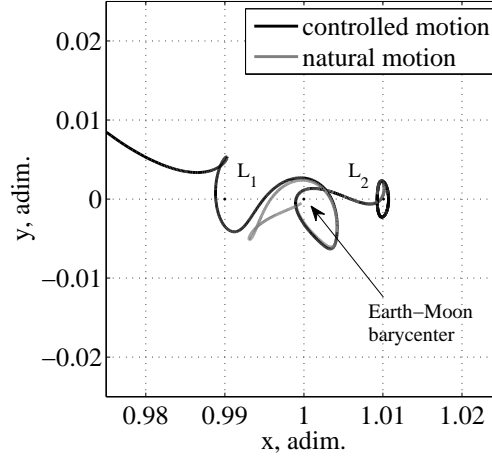
29

Figure 17: Visualization of the selected solution and the natural motion in the synodic frame.

Table 6: Heliocentric graveyard orbits disposal options selected for Gaia (numerical approach).

	2019/07/02	2020/03/07	2020/11/15	
Epoch	12:11:49.84	09:50:35.17	08:57:24.13	UTC
ΔV^* (ΔV)	0.54 (0.43)	0.00218 (0.00195)	0.29 (0.23)	m/s
m_p	0.29	1.19×10^{-3}	0.16	kg
ΔV–Sun angle	91.94	110.08	89.89	deg
η	80.37	89.36	77.91	%

As can be seen, although the closest approach with the Earth is lower than 0.05 AU (about 0.018 AU), the motion is always confined to the exterior region and the Hill's curves are permanently closed at L_2.

6. Conclusions

The EoL disposal of LPO missions is turning into a relevant problem to be tackled to guarantee a sustainable use of space. As the implementation of disposal options can require a significant amount of propellant, this work suggests that EoL disposal strategies shall be identified and adequately ana-
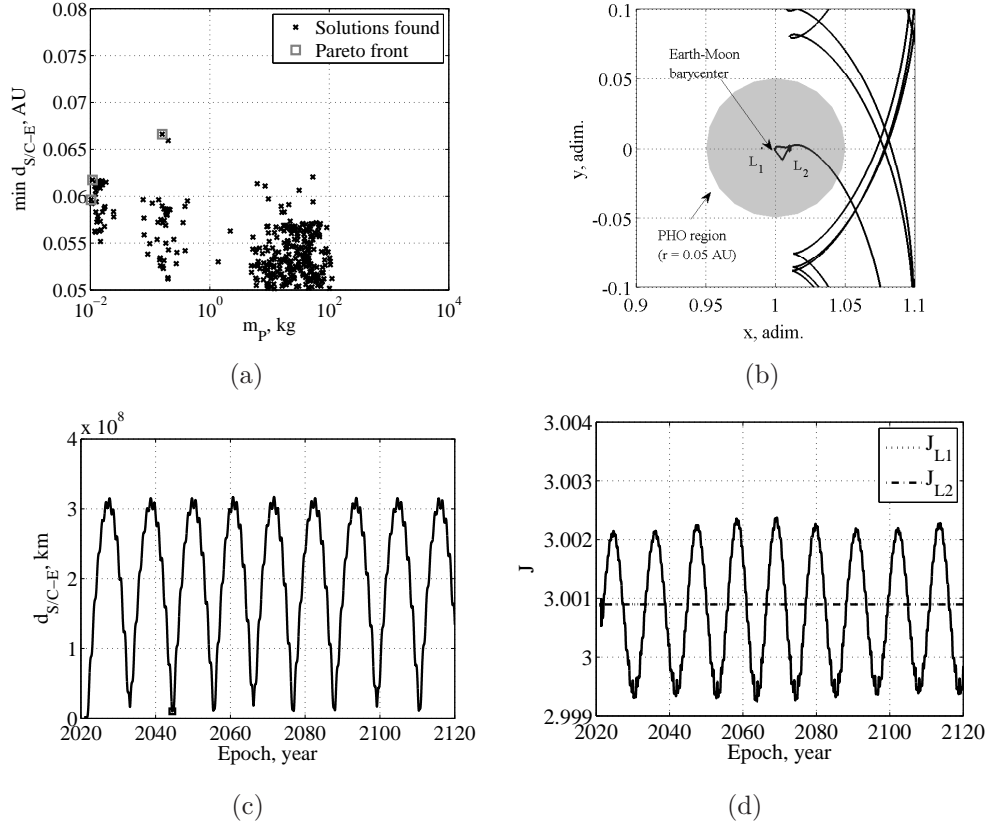
Figure 18: Heliocentric graveyard orbits computed with the numerical approach in the interval from 1 Jun 2020 to 31 Dec 2020: (a) Optimal solutions and Pareto front; (b) Trajectory visualization in the synodic frame; (c) Distance from the Earth (the square highlights the minimum); (d) Jacobi integral profile.

lyzed in the early stages of mission design. To this aim, particular care must be devoted to predict the spacecraft conditions at the beginning of the disposal phase, which must adequately represent the real scenario at the end of the nominal mission lifetime. This analysis was performed for Gaia mission, which has been used as test case throughout the paper.

Three different disposal options were studied, namely Earth re-entry, lunar impact, and heliocentric graveyard orbits. In the latter case, two approaches were developed: a fully numerical approach and an energetic approach. For each option, the disposal maneuvers strategy is defined to maximize robustness while limiting operational complexity and taking into account mission

Table 7: Heliocentric graveyard orbits disposal option selected for Gaia (energetic approach).

Epoch	2020/2/19 23:45:01.74	UTC
ΔJ	7.882185×10^{-5}	–
ΔV_1^* (ΔV_1)	10.52 (8.76)	m/s
$m_{p,1}$	5.73	kg
ΔV_1–Sun angle	93.91	deg
η_1	83.29	%
$\min(J)$	3.000822	–
ΔV_2^* (ΔV_2)	73.55 (41.82)	m/s
$m_{p,2}$	39.44	kg
ΔV_2–Sun angle	52.81	deg
η_2	56.85	%
$\min(d_{S/C-E})$	4.930×10^6	km
m_p	45.17	kg
ToF	180	days
$\min(d_{S/C-E})$	0.018	AU

constraints. The transfer to graveyard orbits using the numerical approach tends to supply more efficient solutions in terms of propellant consumption, which helps identifying feasible trajectories even in the last part of the admissible disposal windows. Being based on a single-maneuver approach, this solution minimizes also the operational complexity. However, it is worth highlighting that this strategy is based on the result of a 100-year numerical propagation and, unlike the energetic approach, it is not able to confine the spacecraft motion to the exterior region of closed Hill's curves. This tends to decrease its robustness to uncertainties on initial conditions and dynamical perturbations. On the other end, the energetic approach requires considerably more propellant to guarantee a safer disposal, which strongly reduces the set of feasible disposal trajectories up to the point that other strategies may be preferable.

Earth re-entry and lunar impact strategies show comparable performances in terms of propellant consumption and they both have the advantage of
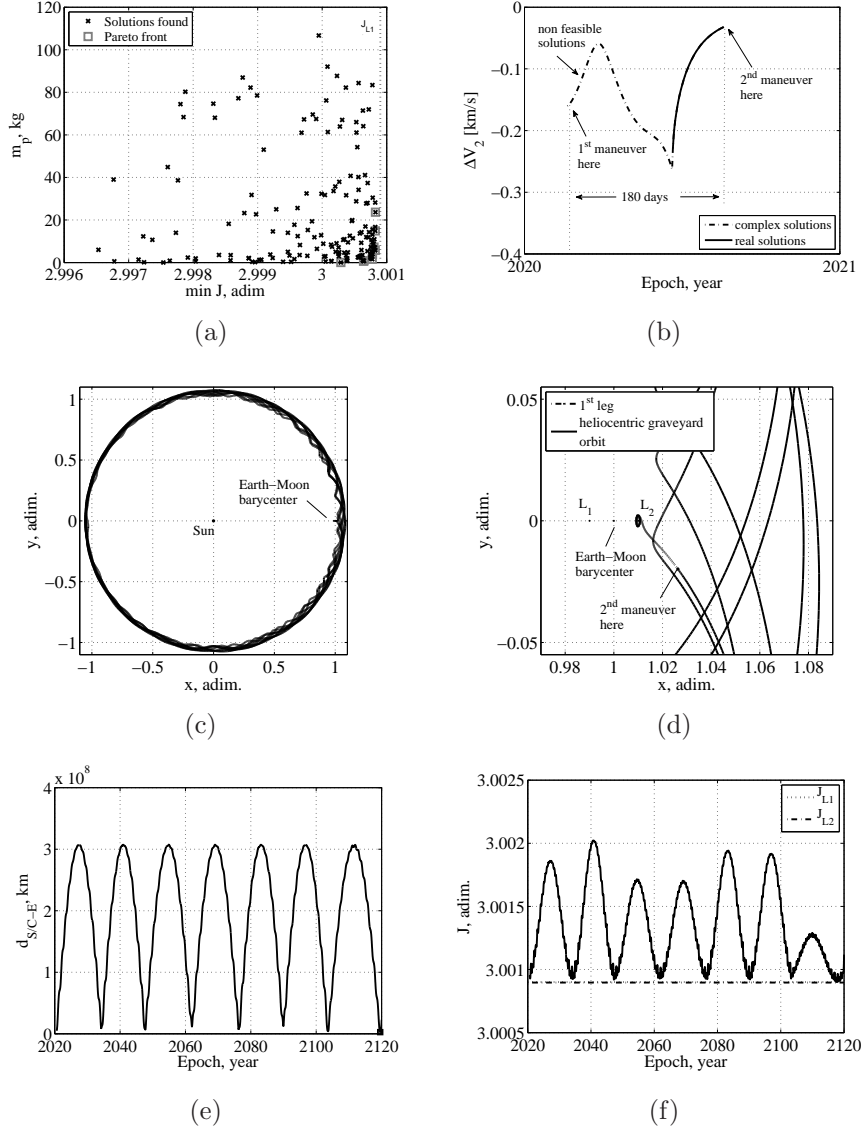
Figure 19: Heliocentric graveyard orbits computed with the energetic approach in the interval from 1 Jan 2020 to 31 May 2020: (a) Optimal solutions and Pareto front for the first maneuver; (b) Analysis of the ΔV_2; (c) Trajectory in the synodic frame; (d) Zoomed view of the trajectory; (e) Distance from the Earth; (f) Jacobi integral profile.

entailing the physical elimination of the spacecraft at the end of its life. Nevertheless, when the Earth re-entry strategy is adopted, the set of feasible

solutions gets considerably smaller for late disposals. Consequently, earlier solutions shall be adopted in this case, which increases also maneuver efficiency.

Future work shall be devoted to carry out a more accurate analysis of all disposal options, including aspects such as the fulfilment of the mitigation requirements for the Earth re-entry and the lunar impact strategies and the resulting stringent control/navigation requirements. Furthermore, sensitivity analyses to uncertainties in initial conditions, maneuver implementations, and model parameters shall be performed to assess the disposal robustness. These additional analyses may play a key role in the identification of the best disposal option.

7. Acknowledgments

References

Akioka, M., Nagatsuma, T., Miyake, W., Ohtaka, K., Marubashi, K., The L5 mission for space weather forecasting. Advances in Space Research 35 (1), 65–69, 2005.

Alessi, E. M., Colombo, C., Landgraf, M., Re-entry disposal analysis for libration point orbit missions. 24th International Symposium on Space Flight Dynamics - ISSFD 2014, Laurel, MD, USA, 5–9 May, 2014.

Armellin, R., Di Lizia, P., Di Mauro, G., Rasotto, M., Landgraf, M., Disposal strategies for spacecraft in lagrangian point orbits. 24th AAS/AIAA Space Flight Mechanics Meeting, Santa Fe, NM, USA, 26–30 January (AAS 14–323), 2014.

Armellin, R., Lavagna, M., Multidisciplinary optimization of aerocapture maneuvers. Journal of Artificial Evolution and Applications 2008, 6, 2008.

Bastante, J. C., Peñin, L., Caramagno, A., Bello-Mora, M., Rodríguez-Cannabal, J., Satellites formation transfer to libration points. Libration Point Orbits and Applications, 455–470, 2003.

Canalias, E., Cobos, J., Masdemont, J. J., Impulsive transfers between Lissajous libration point orbits. The Journal of the Astronautical Sciences 51 (4), 361–390, 2003.

Colombo, C., Letizia, F., Soldini, S., Lewis, H., Alessi, E. M., Rossi, A., Vetrisano, M., Van der Weg, W., Vasile, M., End-of-Life Disposal Concepts for Lagrange-Points and HEO Missions. Final Report. ESA ITT AO/1-7210/12/F/MOS, 2013.

Colombo, C., Letizia, F., Soldini, S., Lewis, H., Alessi, E. M., Rossi, A., Vetrisano, M., Van der Weg, W., Vasile, M., Landgraf, M., End-of-life disposal concepts for libration point orbit and highly elliptical orbit missions. Acta Astronautica, in press.

Deb, K., Evolutionary algorithms for multi-criterion optimization in engineering design. Evolutionary Algorithms in Engineering and Computer Science 2, 135–161, 1999.

Di Mauro, G., Rasotto, Armellin, R., Di Lizia, P., M, Madakashira, H. K., Lara, M., San-Juan, J. F., End-of-Life Disposal Concepts for Lagrange-Points and HEO Missions. Final Report. ESA ITT AO/1-7210/12/F/MOS, 2013.

ESA, Requirements on space debris mitigation for ESA projects. ESA/ADMIN/IPOL(2008)2, Annexes 1, Paris, 1 April, 2008.

Farquhar, R. W., Comments on "Optimal controls for out-of-plane motion about the translunar libration point". Journal of Spacecraft and Rockets 8 (7), 815–816, 1971.

Garcia, L., Farquhar, R., Eastman, T., New opportunities for a historic spacecraft. Space Weather 10 (8), 1–2, 2012.

Hechler, M., Cobos, J., d'Aiguablava, P., Herschel, Planck and Gaia orbit design. Libration Point Orbits and Applications, 115–135, 2002.

Kennedy, J., Eberhart, R. C., Swarm Intelligence. Morgan Kaufmann Publishers Inc., San Francisco, CA, USA, 2001.

NASA, 2011. NASA's recommendations to space-faring entities: How to protect and preserve the historic and scientific value of U.S government lunar artifacts. Available on www.nasa.gov/directorates/heo/library/reports/lunar-artifacts.html

Olikara, Z., Gómez Muntané, G., Masdemont Soler, J., End-of-life disposal of libration point orbit spacecraft. 64th International Astronautical Congress, Beijing, China, 23–27 September (IAC-13.C1.82.), 2013.

Prado, A. F. B. A., Impulsive transfers to/from the lagrangian points in the Earth-Sun system. Libration Point Orbits and Applications, 239–252, 2002.

Renk, F., Landgraf, M., Gaia: Trajectory design with tightening constraints. 24th International Symposium on Space Flight Mechanics - ISSFD 2014, Laurel, MD, USA, 5–9 May, 2014.

Schmidt, M., Keck, F., The end of life operations of the Herschel space telescope. AIAA SpaceOps2014 Conference, Pasadena, CA, USA, 5–9 May (AIAA 2014-1935), 2014.

Seidelmann, P. K., Explanatory supplement to the astronomical almanac. University Science Books, Mill Valley, California, 2006.

Szebehely, V., Theory of orbits: the restricted problem of three bodies. Academic Press, London, 1967.

Szebehely, V., Williams, C. A., Collinear libration points. The Astronomical Journal 69, 460–470, 1964.

UN, 2002. United Nations treaties and principles on outer space. Available on www.unoosa.org/pdf/publications/st_space_11rev2E.pdf